# Low-temperature spectroscopic studies of single molecules in 3-D and on 2-D hosts

Smit, R.

# 4

# SINGLE MOLECULES IN A 2-D ELECTRIC FIELD

*In this chapter a new host matrix for terrylene molecules, called [1]BenzoThieno[3,2-b]BenzoThiophene or shortly BTBT, is the center of study. We show that the insertion of terrylene inside a single crystal of BTBT leads to a non-centrosymmetric arrangement of host molecules around the terrylene molecule. In experiments, this comes forward by a moderately strong linear response to an electric field, caused by a change in dipole moment between ground and excited state of about 0.28 ± 0.09 Debye. In order to additionally resolve the direction of permanent dipole moments between the ground and excited state we made use of a simple geometry of electrodes that allowed us to direct an electric field at all in-plane angles.*

The contents of this chapter are published in: R. Smit, Z. Ristanovic, I. Deperasinksa, B. Kozankiewicz and M. Orrit, Probing the in-plane dipole moment vector between ground and excited state of single molecules by the Stark effect, ChemPhysChem 2024, e202300881

# 4.1. INTRODUCTION

## 4.1.1. THE STARK EFFECT

Using molecular probes to sense electric fields at the nanoscale is a well-studied technique that started with cell membranes[1] and hole-burning experiments.[2] The interaction of a fluorescent molecule with an electric field manifests itself through a linear and/or quadratic shift of the optical resonance with field strength. The total shift of the optical resonance in an electric field perturbation is expressed as follows:

$$h\Delta\nu = -\Delta\vec{\mu}.\vec{E} - \frac{1}{2}\vec{E}.\Delta\overleftrightarrow{\alpha}.\vec{E}, \tag{4.1}$$

where $\Delta\vec{\mu}$ is the permanent dipole moment vector and $\Delta\overleftrightarrow{\alpha}$ is the polarizability tensor, both measured as the difference between those quantities in the ground and excited state.



Usually, the quadratic Stark effect is dominant in the case the molecule under study is centrosymmetric, which is the case for the commonly-studied molecules in cryogenic single-molecule spectroscopy. Moreover, the quadratic Stark effect is always (ignoring exotic exceptions) negative and therefore the molecule's resonance can only shift in one direction. This is not a constraint for the linear component of the Stark effect, but it requires non-centrosymmetry. This can be achieved in two ways. One of them is changing the structure of the molecule by chemical substitutions, such that symmetry is broken.[3] However, chemical substitutions may lead to unfavourable changes in photophysical properties, such as an increased intersystem crossing rate and/or changes in triplet lifetimes. Another possible consequence of chemical substitutions is an increased electron-phonon coupling, which can negatively influence the strength of the zero-phonon line.[3] The alternative to chemical substitutions is the insertion of the centrosymmetric molecule into an environment consisting of a non-centrosymmetric arrangement of host molecules. This so-called host- or matrix-induced asymmetry has proven to yield the best of both worlds and effectively maintains the photophysical properties of the guest. For dibenzoterrylene (DBT), doped into a 2,3-dibromonapthalene (DBN) matrix, the symmetry-breaking property of the host leads to a high linear Stark coefficient of 1.5 GHz/(kVcm$^{-1}$) at a narrow lifetime-limited linewidth of about 37 MHz.[4] Even higher linear Stark shifts have been observed in semi-crystalline polyethylene doped with terrylene.[5] However, unlike the aforementioned DBT in a DBN crystalline matrix, the linear Stark coefficients in the polymer matrix were broadly distributed due to disorder, while the optical resonances of the molecules were unstable.[6]

The sensitivity of molecules to electric fields, for instance for DBT in DBN, is large enough to detect a single charge at a distance of a few hundred nanometer and could compete with the charge sensitivity of single-electron transistors,[7–9] while avoiding complex fabrication techniques. Moreover, with many molecules as electric field sensors inside the crystal, a charge could in principle be triangulated by mapping its electric field.[7] However, despite narrowly-distributed linear Stark coefficients, the dipole vectors of single molecules can orient in several directions due to symmetry of the insertion site. In the case of DBT in DBN this results for instance in four different in-plane orientations,[4] which are spectroscopically equivalent and typically hard to distinguish

with polarized excitation. In order to reliably triangulate single electrons or map electric fields by both direction and magnitude, the specific orientation of each molecule's dipole vector would have to be known.

In this work, we examine a method to determine for each molecule the angle and magnitude of the dipole vector. Using a quadrupole arrangement of electrodes we vary the direction of a mesoscopic electric field and measure the frequency shift of the molecule. This particular arrangement of electrodes has for instance been applied to defects in SiC[10] or on NV centers in diamond.[11] To test this proof of principle on molecular crystals, we performed these experiments on a novel host matrix for single terrylene molecules, namely unsubstituted [1]BenzoThieno[3,2-b]BenzoThiophene, which will be abbreviated as BTBT from now on. We will show that the insertion of terrylene into a BTBT single crystal leads to a relatively strongly broken symmetry, inducing a dipole moment between ground and excited state of terrylene by about 0.28 ± 0.09 Debye. We complement our study by measurements of the spectroscopic and photophysical properties of terrylene in this new host matrix. Furthermore, we determine the orientation of terrylene molecules with polarized excitation and link these studies to quantum chemistry calculations on possible insertion sites for terrylene.



## 4.2. EXPERIMENTAL

### 4.2.1. CRYSTAL PREPARATION AND TRANSFER

BTBT was synthesized and purified by prof. Boleslaw Kozankiewicz from the institute of Physics in Warsaw. All the procedures of synthesis and purification of BTBT are described in this paper.[12] Single crystals of BTBT doped with terrylene were obtained through co-sublimation in a 0.2 bar argon gas atmosphere at a temperature of about 200 ˚C, slightly below the melting point of BTBT (217-218 ˚C). The grown crystals have the form of thin plates of a few tens of μm thick and a surface area of about 10 $mm^2$. The fragile BTBT crystals were picked up with a sharp glass tip and deposited on the sample. With a small droplet of vacuum grease (Apiezon) it was made certain that the crystals remained in place during the cooldown with liquid helium.

### 4.2.2. PREPARATION OF QUADRUOPLE ELECTRODES

The four electrodes (see Figure 4.8) were patterned by e-beam lithography on a $SiO_2$-coated (300 nm) p-doped Si wafer (University Wafer) covered with a spin-coated bi-layer resist (400 nm PMMA 600 kDa and 250 nm PMMA 950 kDa). Both layers were cured for two minutes on a hot plate at 180 ˚C. After development of the exposed patterns and submersion in a 1:3 MIBK:IPA solution for 30 seconds, the structures were established by evaporating a 5 nm Cr adhesion layer and an 80 nm Au layer. Excess metal was removed by lift-off in heated acetone (45 ˚C) under continuous stirring. The metal pads were designed to be 0.75 mm apart from the junction area in order to avoid the optical objective from potentially shorting the Al wires (50 μm diameter) that were bonded between 200 $\mu m^2$ gold pads and their corresponding connections to the sample holder. The sample holder itself was connected to two analog

outputs of an Adwin Gold DAQ card. The remaining two electrodes were shorted with the ground plane.

### 4.2.3. CONFOCAL FLUORESCENCE MICROSCOPY SETUP

The measurements were acquired in a liquid-helium flow cryostat (Janis, SVT-200-5) that can reach a base temperature of 1.2 K. The samples were illuminated through a microscope objective (0.85 NA, Edmund Optics) immersed in the liquid helium, that forms a part of a home-built confocal setup. For the excitation we used a tunable Coherent 699 dye ring laser operated with Rhodamine 6G dye and pumped by a Coherent Verdi V2 laser (5 W at 532 nm). The effective tuning range extended from 560 to 620 nm, while the output wavelength was continuously monitored using a High Finesse WS6-200 wavemeter. Fluorescence was separated from the excitation light by a 615 LP filter (Chroma) and detected by either one or two (for Hanbury-Brown and Twiss experiments) avalanche photodiodes (Excelitas, SPCM-AQRH-16). Fluorescence spectra were recorded with a Horiba iHR320 spectrometer coupled to a liquid-nitrogen-cooled Symphony II CCD detector. Time-correlated single-photon counting was performed using a PicoHarp 300 from PicoQuant. For the start-stop experiments, a delay was imposed on the stop channel by a programmable delay box (Ortec DB463). The linear polarization of the excitation beam was controlled with a half-wave plate (Thor Labs, 588 nm zero-order) after cleaning up with a linear polarizer. The polarization state of the excitation beam was directly measured using a polarization analyzer (Schäfter+Kirchhoff SK010PA).

## 4.3. RESULTS AND DISCUSSION

### 4.3.1. LINE-NARROWING SPECTROSCOPY

The chemical structure of BTBT in Figure 4.1 shows that BTBT is an elongated aromatic molecule composed of two centro-symmetrically arranged thiophene rings in between two benzene rings. The origin of the optical absorption of BTBT was measured to be around 367.3 nm and the origin of the phosphorescence spectrum was found at 483 nm.[12] Therefore both the singlet and triplet excited states of BTBT are higher in energy than the singlet excited state of terrylene (typically around 580 nm), avoiding quenching of the guest singlet by energy transfer to the host's singlet or intermolecular intersystem crossing to the host's triplet.[13] A fluorescence spectrum of an ensemble of terrylene molecules in BTBT reveals the existence of at least two spectroscopic sites (Figure 4.1). Multiple spectroscopic sites are not unusual for terrylene in aromatic host matrices and were for example also found for terrylene in *para*-dichlorobenzene,[14] anthracene[13] and *p*-terphenyl.[15] The two sites we find are a blue site with origin around 16,869 $cm^{-1}$ (593.0 nm) and a red site around 16,620 $cm^{-1}$ (601.9 nm).

Based on the spectral intensities and the concentration of emitters in the fluorescent images of BTBT crystals, the red site appears to have a much higher population than the blue site (see Figure 4.2). In addition, the blue site is typically characterized by a strong background, which is likely caused by a coincidence of the vibronic line at

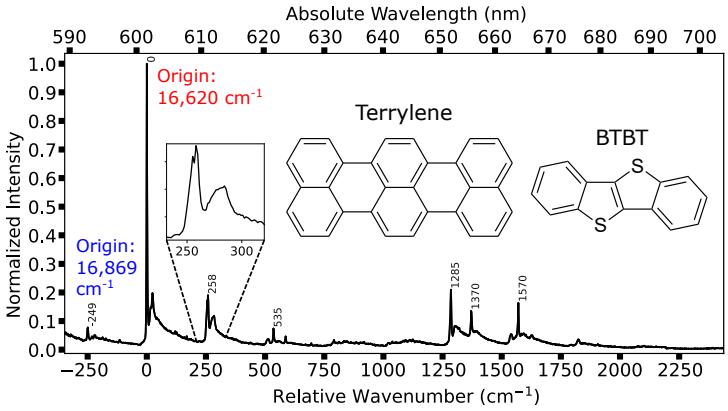


Figure 4.1.: Fluorescence spectrum of an ensemble of terrylene molecules in a BTBT host crystal, excited through a vibronic transition at a wavelength of 582.5 nm. The 0-0 ZPL of a red site peaks at 16,620 $cm^{-1}$ (601.9 nm). Note that a feature on the blue side of this line arises from molecules in a blue site: origin at 16,869 $cm^{-1}$ (593.0 nm). The Debye-Waller factor of the ensemble, as the ratio of the intensity of the 0-0 ZPL to the sum of the intensity of the 0-0 ZPL and the phonon side band, is 0.27 ± 0.03.

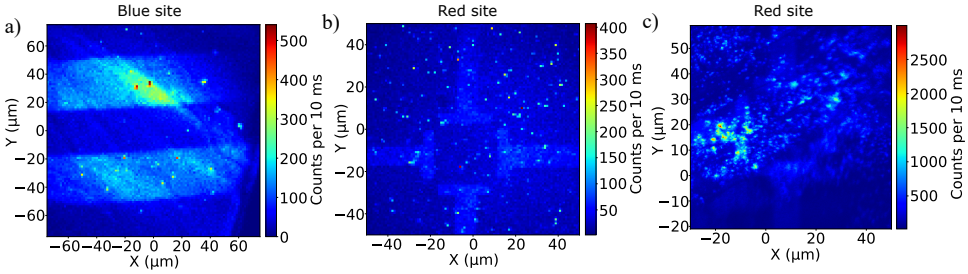


Figure 4.2.: Fluorescence maps of BTBT crystals, measured at different excitation wavelengths. In panel (a) the excitation wavelength was 591.95 nm. Panel (b) is taken at 604.2 nm and panel (c) is taken around 601.3 nm. The image in (a) corresponds to molecules in the blue site, while (b) and (c) are corresponding to the red site. Note that the concentration of fluorescent spots is much higher for (b) and (c), while the background is high in (a).

258 $cm^{-1}$ of the red site with the 0-0 zero-phonon line (ZPL) of the blue site. This coincidence is noticeable from the fluorescence emission spectrum in Figure 4.1. The sharp peak is the 0-0 ZPL of the red site, while a weak signal from the blue site is visible around -249 $cm^{-1}$. The difference in wavenumbers between the two sites is indeed very close to the red site's strong vibronic line around 258 $cm^{-1}$. Noteworthy

is that the red site's spectral position is most red-shifted compared to previous studies of terrylene, where the most red-shifted site was obtained in para-dichlorobenzene at 597 nm.[14] Furthermore, the red site's spectrum shows a splitting of the main vibronic line at 255-258 $cm^{-1}$. Such a splitting could be a signature of non-planar distortion of terrylene's molecular structure due to insertion in the BTBT crystal, which was similarly observed for terrylene in naphthalene,[16] though with a more pronounced splitting of 13 $cm^{-1}$. As the red site is the most convenient site to study in terms of background, a high population of terrylene molecules and as we will show next, a better spectral stability as well, we will focus in our studies mainly on the red site.

### 4.3.2. PHOTOPHYSICAL PROPERTIES OF TERRYLENE IN BTBT



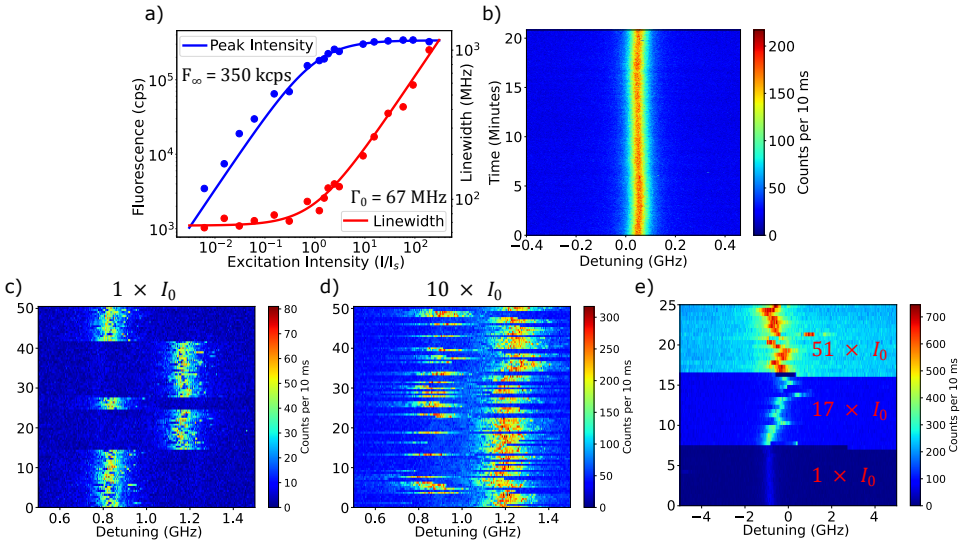


Figure 4.3.: Spectral properties of single terrylene molecules. Panel (a) shows the linewidth and fluorescence rate covered over four orders of magnitude in laser intensity for a molecule in the red site, shown here along with fits of the saturation intensity $I_s$. The estimated saturation intensity is in the order of 2 $W/cm^2$. The red data points are the measured linewidths, which are fitted to the broadening equation $\Gamma(I) = \Gamma_0\sqrt{1 + I/I_s}$. The blue data points are the measured fluorescence rates as a function of laser intensity, fitted to $F(I) = F_\infty(I/I_s)/(1 + I/I_s)$. Panel (b) shows another molecule in the red site that was followed in real time for more than 20 minutes with an integration time of 10 ms per point. Panel (c) and (d) show a molecule in the blue site that couples to a two-level system (TLS), that induces spectral jumps in the series of excitation spectra. Typical for TLSs, the jump rate scales with the excitation intensity. Panel (e) shows a molecule in the blue site that undergoes spectral diffusion upon increasing excitation intensities.

As typically reported for terrylene-doped single-crystal matrices, most terrylene molecules show an excellent spectral stability over longer time.[14,15,17] One example of a spectrally-stable terrylene molecule is given in Figure 4.3b, which shows no spectral diffusion over the measured time of about 20 minutes. Most molecules in the red site are as stable as the molecule in Figure 4.3b, while unstable molecules tend to be more abundant in the blue site. These instabilities are particularly characterized by spectral jumps due to the presence of (tunnelling) two-level systems (see Figure 4.3c and 4.3d). Furthermore, spectral diffusion at excitation intensities beyond saturation is present in the blue site (Figure 4.3e). This might point to a photo-induced separation of charges in the host crystal.[18]

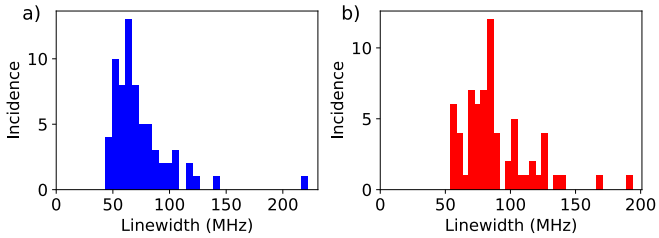


Figure 4.4.: Distributions of homogeneous linewidths of molecules in the blue site for panel (a) and molecules in the red site for panel (b). The excitation intensity was kept below typical saturation intensities to avoid power broadening of the resonances.

The homogeneous linewidth for the molecule in Figure 4.3a is about 67 ± 5 MHz, which is slightly broader than the narrowest linewidths found for terrylene in the red site: about 54 MHz (see distribution of linewidths for the blue and red site in Figure 4.4). However, a linewidth of 54 MHz remains broader than what is expected from typical lifetime-limited terrylene molecules reported in other matrices: ranging from 35 up to 45 MHz.[17,19] To determine whether the homogeneous linewidth of 54 MHz is close to the lifetime-limited value, we performed antibunching measurements on single molecules in a Hanbury-Brown-Twiss configuration. We recorded the coincidence histogram of the emitted fluorescence photons with the laser at resonance with the 0-0 ZPL using a 256 ps binning time, while delaying the stop-pulse by 36 ns. As expected, Rabi oscillations appear at high laser intensities, shown in Figure 4.5.

Since the detection efficiency of our setup is around $10^{-3}$, as determined previously in Chapter 2, we can relate the coincidence histograms, for the given time frame, directly to a correlation function.[21] The correlation function for photons can be found by solving the optical Bloch equations with the Laplace transform (see derivation in Appendix 1), where we ignored contributions from the triplet state, which only adds photon bunching at longer timescales. The background causes a deviation from zero at the dip and can be taken into account by using the relation: $g_B^{(2)}(\tau) = 1 + \frac{1}{(1+\frac{B}{<I>})^2}(g^{(2)}(\tau) - 1)$, where $g_B^{(2)}(\tau)$ is the autocorrelation function that includes background, captured by the term $B$

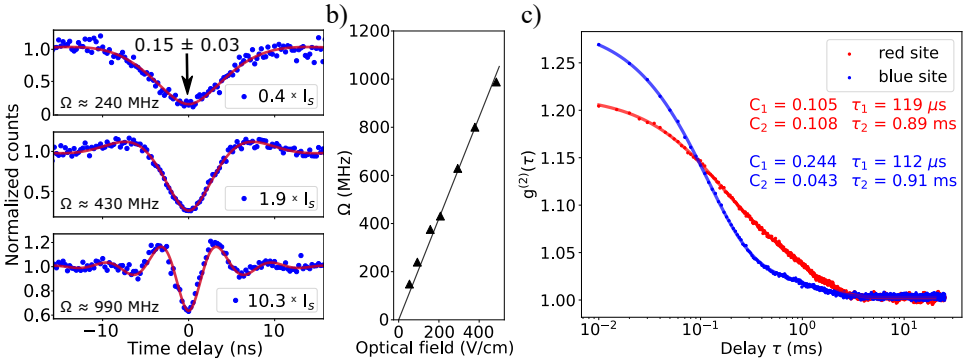


Figure 4.5.: Antibunching measurements on a single terrylene molecule at resonance with the 0 0 zero-phonon line, recorded for around 5 minutes per histogram. The three figures correspond to different excitation intensities, as units of the saturation intensity of about 2 $W/cm^2$, where the fitted Rabi frequencies are given by Ω. The red curves are fits of the experimental data to equation 4.2. The data and fit were normalized to approach unity at timescales » $T_2$. b) Fitted Rabi frequencies Ω as a function of the estimated optical field intensity at the center of the focused Gaussian beam, using the relation $\Omega = |\mu_{12}||E_{opt}|/\hbar$. The optical field intensities were estimated by $|E_{opt}| = \sqrt{(4\eta P/(\pi w^2))}$, with $\eta = \sqrt{\mu_0/(\epsilon_0\epsilon_r)}$ being the wave impedance with $\epsilon_r \approx 3$, $P$ the laser power corrected for losses and $w$ the beam waist of about 500 nm. Neglecting an angle between the transition dipole moment $\mu_{12}$ and the optical field $E_{opt}$, the estimated transition dipole moment is about 1 Debye. Later, we will show that the transition dipole moment is estimated to be around 9.4 Debye using quantum-chemistry calculations. The deviation could be partly explained by the usual overestimation of the saturation intensity with respect to the true optical field at saturation.[20] c) Fluorescence-autocorrelation functions reveal bunching at the µs to ms time scale due to intersystem crossing (ISC) to the triplet state. The two curves represent data of single molecules in the red and blue sites, taken at about 3 times the saturation intensity. The data was fitted to a bi-exponential decay of the form $g^{(2)}(\tau) = C_1 \exp(-\tau/\tau_1) + C_2 \exp(-\tau/\tau_2)$, with the obtained parameters for both sites displayed in the image. The fit parameters show a clear difference in contrasts $C_1$ and $C_2$ among the two sites, while characteristic time scales for $\tau_1$ and $\tau_2$ are almost equal.

in relation to the average fluorescence signal $< I >$. Finally, the normalized coincidence histograms were fitted to the following correlation:[19,22]

$$g_B^{(2)}(\tau) = 1 - \frac{1}{(1+\frac{B}{<I>})^2}\exp\left(-\frac{|\tau|}{2}(\pi\Gamma_0+\gamma_{21})\right)\times\left[\left(\frac{\pi\Gamma_0+\gamma_{21}}{2\tilde{\Omega}}\right)\sin\left(\tilde{\Omega}|\tau|\right)+\cos\left(\tilde{\Omega}|\tau|\right)\right], \tag{4.2}$$

with $\gamma_{21} = 1/T_1$ the decay rate of the excited state, $\pi\Gamma_0 = 1/T_2$ as the inverse of the coherence or dephasing time, and $\tilde{\Omega} = \frac{1}{2}\sqrt{4\Omega^2 - \gamma_{21}^2 - (\pi\Gamma_0)^2 + 2\pi\Gamma_0\gamma_{21}}$, where $\Omega$ is the Rabi frequency ($\Omega = |\vec{\mu}_{12}\vec{E}_{opt}|/\hbar$). The slope of the exponential following the dip is given by a sum of parameters that depend on $T_1$ and $T_2$, which makes them difficult to separate from the antibunching measurements alone. Hence, we relate $T_2$ to the homogeneous linewidth $\Gamma_0$ = 54 MHz, which we obtained from the excitation spectra, through the relation $T_2 = 1/\pi\Gamma_0$. For four molecules, we measured and fitted antibunching curves at a range of excitation intensities, which results in an average excited state lifetime $T_1 = (\gamma_{21})^{-1}$ of 3.0 ± 0.2 ns. When calculating the lifetime-limited linewidth by $\Gamma_0 = 1/(2\pi T_1)$, the result corresponds to a linewidth of 53 ± 4 MHz, which indeed is close to the smallest linewidths found in this system and shows there is very limited additional decoherence. Nevertheless, this lifetime is on the short side for what was reported for terrylene in other systems, with 3.15 ns being the shortest lifetime measured for terrylene in anthracene.[23] The shortened lifetime for terrylene in anthracene was explained by both an enhanced intersystem crossing through the host's triplet and a high refractive index of the anthracene host. Although no report of refractive indices for BTBT can be found, derivatives of BTBT, such as the less-dense polymerized C8-BTBT were reported to have high refractive indices of 1.74 and 1.6 along the out-of-plane and in-plane axes.[24] These refractive indices are relatively close to the refractive indices of anthracene.[25,26] The reduced lifetime of terrylene might therefore be related to a high refractive index of BTBT. In addition, a high refractive index, which can cause a stronger van der Waals interaction with the matrix, might (partly) explain the relative red-shift of the spectroscopic sites in BTBT.



At longer time scales of μs to ms, time-correlated single-photon counting reveals the blinking properties of molecules in the two sites. Fluorescence time traces at resonant excitation were recorded and used for the calculation of the autocorrelation function $g^{(2)}(\tau)$. For molecules in both sites we can distinguish two exponential decays (see Figure 4.5c) in the autocorrelation, which are assigned to the in-plane $T_{xy}$-triplet substates for the short decay and the out-of-plane $T_z$-triplet substate for the long decay.[15,27] For the blue site, the $T_z$ component is relatively weak, which is not the case for the red site. The autocorrelations were recorded at different excitation intensities and processed in a global fit (see procedure also in Chapter 2), together with a saturation and linewidth broadening curve such as in Figure 4.3a and Figure 4.6a and 4.6d. Disregarding inhomogeneity in the ISC rates of single molecules within the sites, the difference among the sites is not that significant (see Table 4.1). For example, in a pentacene-doped *p*-terphenyl matrix the ISC rates were varying by over two orders of magnitude among spectroscopic sites.[28] However, the triplet lifetimes we find for the two sites are for both the $T_{xy}$-triplet substate and the $T_z$-triplet substate about a factor 3 shorter than typically reported for terrylene in other matrices, such as *p*-terphenyl[15,29] and terrylene on hBN in Chapter 5. The shorter lifetimes might be the result of a

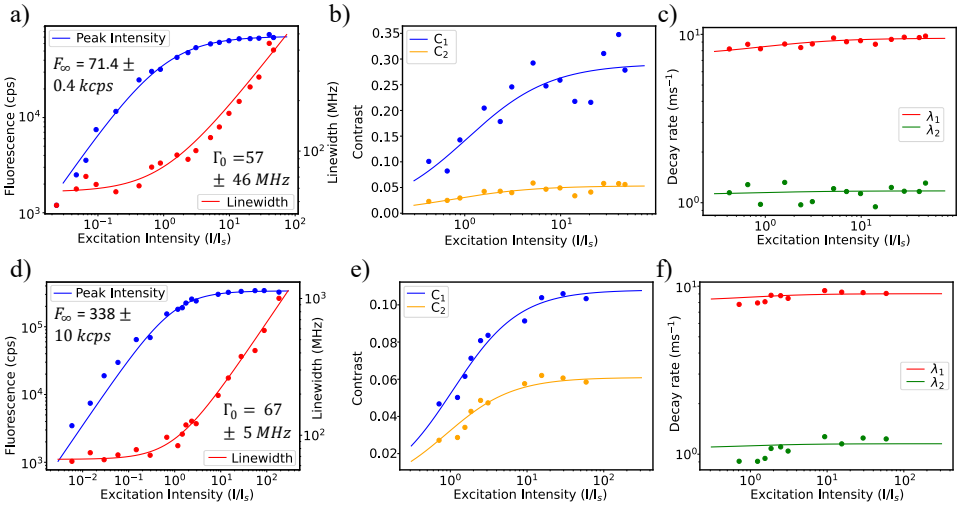


Figure 4.6.: Global fits for the saturation of fluorescence and power broadening of the linewidth are shown in panel (a) and panel (d), combined with fit parameters for the autocorrelation functions, such as contrasts of the exponential decays in panel (b) and panel (e) and decay parameters in panel (c) and panel (f), taken at a range of excitation intensities. The top panels correspond to a molecule in the blue site, while the bottom panels correspond to a molecule in the red site. The resulting parameters obtained from the global fits are displayed in Table 4.1.

heavy-atom effect and/or distortion of the terrylene molecule in its site.

| *Site* | *Position* $(cm^{-1})$ | *Linewidth* : $\Gamma_0$ $(MHz)$ | *ISC rate* : $\gamma_{23}^{xy}$ $(s^{-1})$ | *Lifetime* : $(\gamma_{31}^{xy})^{-1}$ $(\mu s)$ | *ISC rate* : $\gamma_{23}^{z}$ $(s^{-1})$ | *Lifetime* : $(\gamma_{31}^{z})^{-1}$ $(ms)$ |
|---|---|---|---|---|---|---|
| *Blue* | 16,869 | 43 | $4000 \pm 300$ | $134 \pm 3$ | $170 \pm 50$ | $0.9 \pm 0.1$ |
| *Red* | 16,620 | 54 | $1900 \pm 400$ | $125 \pm 15$ | $300 \pm 80$ | $1 \pm 0.2$ |

Table 4.1.: Spectroscopic and photophysical properties of the blue and red site. The intersystem crossing (ISC) rates and lifetimes of the two distinguishable triplet states, are derived from correlation functions $g^{(2)}(\tau)$, recorded at different excitation intensities. Since these parameters for ISC and triplet lifetimes concern single-molecule measurements they may be affected by the inhomogeneity of the molecules' environment.

### 4.3.3. DETERMINATION OF DIPOLE VECTORS WITH A 2-D ELECTRIC FIELD

As explained in section 4.1.1., the linear Stark effect requires a change in the electric dipole moment between ground and excited state, which is a vector: $\Delta\vec{\mu}$. In the regime of voltages that we applied, we observed a moderately strong linear Stark shift with a negligible quadratic component. The dominance of the linear Stark shift is not trivial, as both the BTBT host and terrylene are centrosymmetric. Therefore the change in dipole moment between ground and excited state must be induced by a symmetry-breaking insertion into the host's crystal lattice.[4]

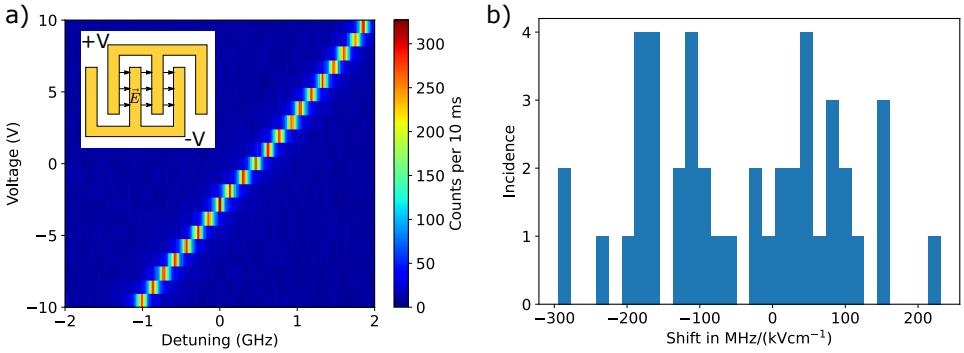


Figure 4.7.: Panel (a) shows the response of a single molecule in the blue site to an incremental electric field between interdigitated electrodes, which are schematically drawn in the figure inset. Panel (b) shows the distribution of Stark coefficients for 44 single molecules that are measured in the same range as the molecule in panel (a).

We started with typical Stark effect measurements, where a set of parallel electrodes are used to impose an electric field in one dimension (see schematic in inset of Figure 4.7a). However, the strength of the measured Stark effect depends on the direction of the dipole vector $\Delta\vec{\mu}$, which due to symmetry of the insertion site can have different projections on the imposed electric field. These projections of $\Delta\vec{\mu}$, together with inhomogeneities of $\Delta\vec{\mu}$ from molecule to molecule due to different charge environments, resulted in a complex distribution of Stark coefficients, as shown in Figure 4.7b.

To reduce the complexity of the measured Stark coefficients, by measuring the Stark effect independently of the alignment of the crystal to the electrodes, we designed a quadrupole structure with four independently-connected electrodes (Figure 4.8a). The crystal is mounted on top of these four electrodes (Figure 4.8b). We apply a bias on the horizontal and vertical electrode pair (Figure 4.8d). With COMSOL simulations in Figure 4.8d we show that the electric field is mostly homogeneous at the center and moreover we find that the superposition principle of the horizontal and vertical electric field applies, which makes it possible to orient the field in all in-plane directions. These

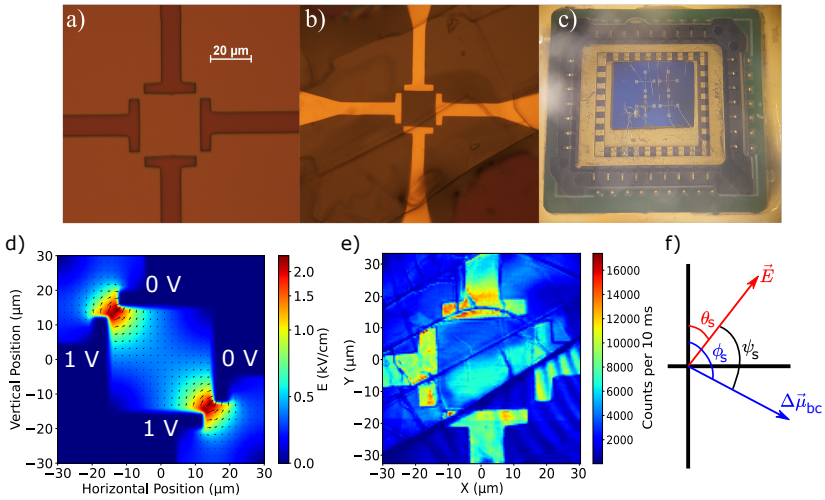


Figure 4.8.: Panel (a) shows the patterned electrodes in the e-beam resist layer. In panel (b) the structures have been filled with gold and a BTBT crystal is mounted on top. The sample is attached to a holder and wire bonded in panel (c) in order to apply voltages to the electrodes. The simulated electric field is shown in panel (d) for a case of symmetric voltages on the horizontal and vertical electrode pairs. Panel (e) shows the confocal reflection image of the mounted crystal that was used in low-temperature experiments. The definitions of the angles used in equation 4.3 are shown schematically in panel (f).

simulations are performed in two dimensions and do not take the substrate or any other anisotropies in the environment into account. Furthermore, the simulations show that the field at the center is a factor 1.2 weaker compared to the naive case where the field is equal to the potential difference divided by the distance between the electrodes (30 µm). This is likely due to concentration of the field between the side tips of the electrodes. The factor of 1.2 was taken into account when fitting experimental data to theory.

As the crystal itself is three-dimensional, the applied electric field is only sensing the projection of $\Delta\vec{\mu}$ in the crystallographic bc-plane, due to the crystalline structure of BTBT.[30] The linear shift of the resonance frequency of the single molecules is given by the scalar product of the two vectors $-\Delta\vec{\mu}.\vec{E}$. Taking into account only the components that are in the plane of the electric field and neglecting crystal anisotropy, the magnitude of the shift reduces to:

$$h\Delta\nu = -|\Delta\vec{\mu}_{bc}||\vec{E}|\cos\psi_s, \tag{4.3}$$

where $\psi_s$ indicates the angle between the dipole moment $\Delta\vec{\mu}_{bc}$ and the electric field $\vec{E}$. When we center our frame of reference around the electric field, given by angle $\theta_s$, and defining an angle for the dipole vector, as $\phi_s$, the angle $\psi_s$ can be written as $\psi_s = \phi_s - \theta_s$ (see Figure 4.8f).

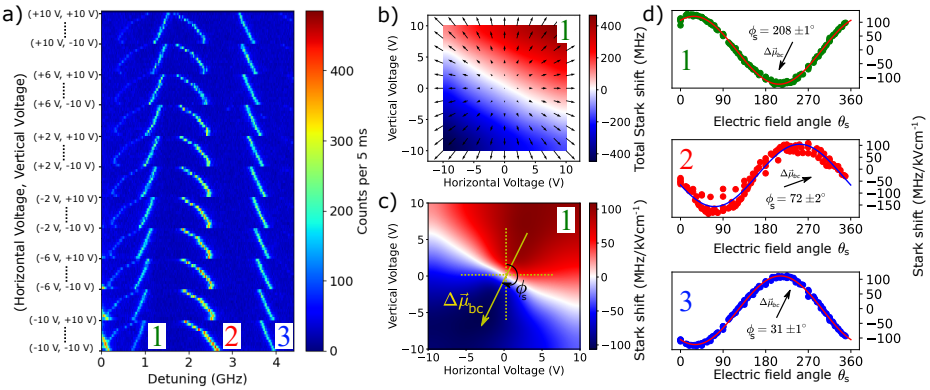


Figure 4.9.: a) Series of 121 single excitation spectra that records the response of molecules in the same focal volume to changing electric field. The scans start with -10 V on both the bottom and left electrode and progresses with a sweep of the voltage on the left electrode from -10 V to 10 V in 11 steps. Subsequently, the voltage on the bottom electrode is increased followed by another sweep of the voltage on the left electrode. Two different patterns can be observed, with molecules moving in both directions. Panel (b) depicts the shift of molecule 1 in (a) for all voltage combinations. The relative magnitude and direction of the applied electric field, in the center between the four electrodes, are plotted as arrows. Panel (c) shows the shifts in (b), normalized for the magnitude of the electric field vector. The direction of the dipole vector and its angle are plotted in the center. (d) The relative magnitude of the Stark effect for the three molecules in (a) is plotted as a function of electric field angle $\theta_s$ and fitted to equation 4.3 as $\Delta\mu/|\vec{E}| = -|\Delta\vec{\mu}_{bc}|\cos(\theta_s - \phi_s) + offset$, where $\phi_s$ is the angle of the dipole vector $\Delta\vec{\mu}_{bc}$. The experimental data in (b) and (c) have been smoothed by bicubic interpolation.

With a predefined step size in voltage, all combinations of horizontal and vertical biases are applied within the range of -10 V to +10 V. For each of the combinations, we recorded an excitation spectrum around the molecule's 0-0 zero phonon line (Figure 4.9a) and fitted this to a Lorentzian distribution to determine its resonance frequency. For all bias combinations, the observed shift of molecule 1 in Figure 4.9a is plotted in Figure 4.9b, where the arrows indicate the electric field direction and magnitude for the corresponding combination of voltages. On the diagonal there is a clear region of white color where little to no shift is observed, even though an electric field is applied. This corresponds to the case where the angle $\psi_s$ is close to 90°. The other diagonal, orthogonal to the white region, represents the direction where the electric field and dipole vector are parallel. On this diagonal, the dipole vector orients in the direction where the Stark shift is negative (equation 4.3). The orientation found for the dipole of

molecule 1 is drawn in Figure 4.9c. For the three molecules in Figure 4.9a, the dipole orients in different directions shown by their relationship with field orientation in Figure 4.9d. Overall, molecule 1 and 3 show good agreement with equation 4.3, while molecule 2 shows more variation. Moreover, the curve of molecule 2 displays a relatively strong asymmetry between positive (up to +100 MHz/(kVcm$^{-1}$)) and negative values (down to -150 MHz/(kVcm$^{-1}$)). In addition, the curve shows nonlinear behaviour for sweeps at different voltage combinations, where the electric field vector points roughly in the same direction, but with a different magnitude (different rows in Figure 4.9b). This may point to an accumulation of charge, which is not observed for molecule 1 and 3. Despite the variations for molecule 2, the angle of the dipole vector can be measured with good accuracy.



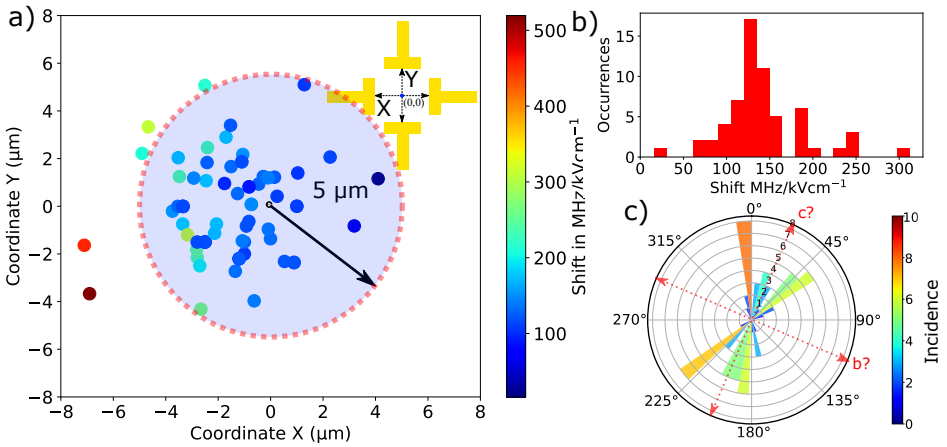


Figure 4.10.: a) Scatter plot of the measured Stark coefficients (maximum shift per unit electric field when the electric field and dipole vector align) of 69 molecules, positioned at their locations with respect to the four electrodes. A circle with radius of 5 µm, drawn from the center between the four electrodes at (0,0), selects the 64 molecules that are closest to the middle and have been plotted in a histogram in panel (b). The distribution of the angles of the dipole vector are plotted in panel (c). Here, the width of the bars indicate the bin size of 9˚ per bin and both the length and color indicate the number of molecules that are present within each bin. The red dashed arrows indicate possible symmetry axes for the dipole vectors, which based on the insertion sites in section 4.3.5 could relate to the noted crystallographic axes (bbc insertion site in Table 4.2).

To gather statistics on the orientation of the dipole vectors in the red site, we performed measurements such as in Figure 4.9 for a total of 69 molecules. The in-plane position of each molecule was measured, such that the molecules close to the center of the four electrodes could be selected. The Stark coefficient of each molecule is

scatter-plotted by its spatial position in Figure 4.10a. From the plot it becomes clear that outliers, in terms of Stark shift, are indeed further away from the center, where there is either a weak or an enhanced field in the gap between the electrodes (Figure 4.8d). Closer to the center position, the spread in values is lower and a histogram of the maximum magnitude of the Stark shift, for molecules inside a circle with a radius of 5 μm, reveals a relatively narrow distribution (Figure 4.10b). The average slope of the Stark shift was measured to be 140 ± 47 MHz/(kVcm$^{-1}$) and this corresponds to an in-plane dipole moment $|\Delta\vec{\mu}_{bc}|$ of 0.28 ± 0.09 Debye, which is not corrected for local-field effects around the molecule.[31] The uncertainty of $|\Delta\vec{\mu}_{bc}|$ can be explained by variations in the electric field further off-center, while also different axial positions of the molecule and charge inhomogeneities around the molecules may contribute to variations of the dipole vector magnitude.



The angle of the dipole moment vector shows a relatively broad distribution (Figure 4.10c). Although these observations are only for the red site, a broad distribution of angles, possibly due to crystal symmetry, may likewise explain the large variations we observed for the magnitude of the Stark effect with a 1-D electric field for the blue site (Figure 4.7b). The distribution for the red site shows that there are at least two populations of molecules, spanning also the opposite quadrant. The drawn dashed lines might be the symmetry axes of the polar distribution. However, the many systems of cracks, possibly also step edges, in Figure 4.8e made it difficult to relate these lines to crystallographic axes. Nonetheless, the observation of a relatively narrow distribution of linear Stark coefficients, and thus non-random orientations for dipole vectors, points to a symmetry that is broken by the host matrix BTBT. This will set a limit to the possible insertion sites. However, an additional method to determine possible insertion sites is by measuring another vector, namely the direction of the transition dipole moment $\vec{\mu}_{12}$. For terrylene, the transition dipole moment follows the long axis, and thus reveals the alignment of the terrylene molecules inside the crystal.

### 4.3.4. THE TRANSITION DIPOLE MOMENT OF TERRYLENE

The transition dipole moment of terrylene, $\vec{\mu}_{12}$, which follows the long axis of the molecule, couples to the optical field $\vec{E}_{opt}$, inducing (Rabi) oscillations between ground and excited state. The coupling between $\vec{\mu}_{12}$ and $\vec{E}_{opt}$ is optimal when the two vectors are parallel. This is achieved by converting the laser light to a linearly-polarized state with a polarizer, while a half-wave plate can tune the angle. As a function of the angle between $\vec{\mu}_{12}$ and $\vec{E}_{opt}$, called $\psi_p$, the fluorescence intensity varies by a $\cos^2(\psi_p)$ relationship.

Before we determined the angle of the transition dipole moment for the crystal in Figure 4.11a, we made sure which crystal cracks represented crystallographic axes, to serve as reference axes for $\vec{\mu}_{12}$. To determine the crystallographic axes we illuminated a BTBT single crystal with white light between crossed-polarizers. As we rotated the crystal, the crystal turned dark at the four angles where the linearly-polarized light aligned with a crystallographic axis. At in-between angles, the crystal was bright and colourful due to birefringence. The extinction angles coincided with the edge of

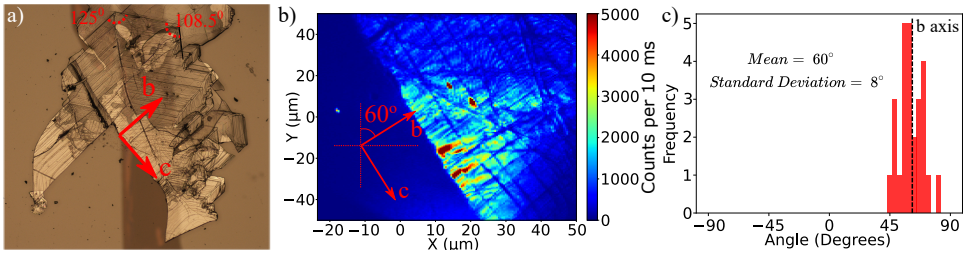


Figure 4.11.: Panel (a) shows a microscope image of the crystal with the annotated crystallographic axes deduced from the structure of the crystal (see angles) and birefringence measurements. Panel (b) shows a confocal microscope image of a part of a BTBT single crystal, taken around the arrows in (a). c) Histogram of the transition dipole moment angle with respect to the axes shown in (b) for 26 different molecules. The average angle is around 60° with a standard deviation of 8°. The angle corresponds to the b-axis, which is perpendicular to the crystal edge.



the crystal and a set of lines perpendicular to the edge, as shown in Figure 4.11b. However, many lines, of which some were possibly step edges, did not coincide with a crystallographic axis and confirm that it is difficult to assign crystallographic axes from series of cracks in the crystals alone.

Single molecules in the red site were excited resonantly by the 0-0 ZPL and their intensity was monitored in the series of excitation spectra, where each line was measured with a different polarization angle (Figure 4.12a and 4.12b). We changed the polarization of the laser light in a range of 180°, which was sufficient to determine the axis of $\vec{\mu}_{12}$. The intensity of the molecule at various polarization angles is fitted to $I(\theta) = B + A\cos^2(\phi_p - \theta_p)$, where $\phi_p$ represents the axis of $\vec{\mu}_{12}$, B the background and A the amplitude. This procedure was repeated for 26 molecules and plotted in a histogram in Figure 4.11c, which shows there is a relatively narrow distribution of transition dipole moments around the b axis, resolved from the outer structure (Figure 4.11a). The same angle of $\vec{\mu}_{12}$ was found at room temperature, where both sites and inhomogeneities have been ensemble averaged (Figure 4.12d). The similarity of BTBT to anthracene, which crystallizes in the same form, supports an insertion of terrylene along the b-axis.[32] An insertion along the b-axis was found for DBT in anthracene, which apart from the two outer benzene rings closely resembles the shape of terrylene.

Taking into account the measured orientation of terrylene along the b-axis of BTBT and the broken symmetry of terrylene by the host, we can start to relate our measurements to a possible insertion site. These calculations were performed by Irena Deperasińska from the Institute of Physics in Warsaw (Poland).

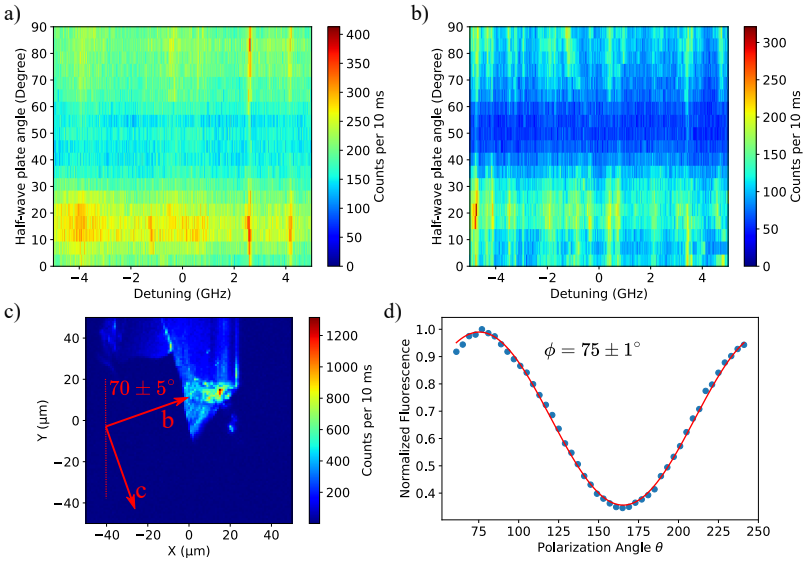


Figure 4.12.: Panels (a) and (b) represent low-temperature excitation spectra of respectively the blue and the red site as a function of half-wave plate angle. Molecules of the two sites follow the same pattern. Panel (c) shows the orientation of the crystallographic axes in a room-temperature measurement. In panel (d) we find a cosine-squared relation of the fluorescence with the polarization angle again. As this measurement was taken at room temperature, different sites cannot be distinguished and this shows that most molecules align with the b-axis. The background does not fully extinguish and may be caused by ill-inserted molecules in the crystal.

### 4.3.5. PROPOSED INSERTION SITES

The equilibrium structure of terrylene inside the BTBT crystal cavities was optimized in the ground ($S_0$) and excited ($S_1$) electronic state with Gaussian16[33] using the procedure ONIOM(B3LYP/6-31G(d,p): PM3), i.e. with the semiempirical PM3 method describing the rigid crystal structure of BTBT and B3LYP and TD B3LYP/6-31G(d,p) methods for terrylene. The cavities inside the BTBT crystal were formed by taking out 2 and 3 BTBT molecules from a crystal element of 48 molecules in a pattern as previously described for DBT in 2,3-dibromonaphthalene[4] and in anthracene crystals.[32] The Franck-Condon factors for the $S_0 \rightarrow S_1$ transition were calculated with a procedure included in Gaussian16. The spin-orbit coupling matrix elements between the singlet and triplet states were calculated with ORCA 4.2.1[34] as square root of the sum of squares of spin-orbit coupling matrix elements of all triplet state sublevels of the uncoupled states.

The calculations on the properties of terrylene in the BTBT host crystal rely on the optimization of the structure of the guest molecule embedded in a cavity obtained by removing the appropriate number of host molecules. In the context of the present work

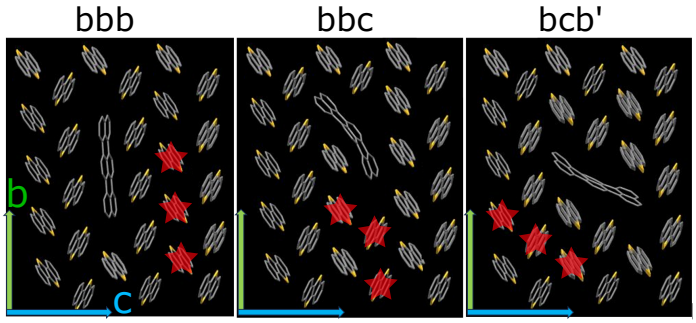


Figure 4.13.: Optimized geometry of terrylene in the three considered cavities, created by the removal of three molecules of BTBT. The red asterisks indicate which molecules have been removed in order to form the cavity for terrylene. The green arrow indicates the b axis and blue the c axis of the BTBT crystal.



our interest is concentrated around the cavities in which terrylene orients with its long axis mostly parallel to the crystallographic b axis. The three possible sites, called bbb, bbc and bcb', are presented in Figure 4.13.

In Table 2, the calculations of terrylene in the three sites are shown. Here, we present the calculated (0,0) transition energies, permanent dipole moments in the $S_0$ and $S_1$ states and the transition dipole moments. Additional calculational results are presented in Tables 3, 4 and 5.

The calculations show that the terrylene molecule loses its planar symmetry. For example, the long axis of the terrylene molecule is slightly longer than twice the distance between BTBT molecules along the b axis, thus a molecule in the cavity bbb is forced to „compensate" this incompatibility by a small deviation from planarity. On the other side, the cavity bbc (Figure 4.13 forces terrylene to be bent in a bow (Figure 4.13), which results in a considerably higher dipole moment than in the two other cases.

In view of the results of the calculations, a lack of planar symmetry of the terrylene molecule is indicated by the appearance of new vibronic lines, absent in the spectrum of isolated (thus planar) terrylene (see Figure 4.14), as well as the appearance of a permanent dipole moment (Table 4.2 and Table 4.4). Other signatures of the symmetry loss are the positive (non-zero) elements of the spin-orbit coupling (Table 4.3).

Out of the three possible cavities occupied by a terrylene molecule, the site bbc seems to be the closest to the experimental red site. Arguments for this assignment are the following:

i) the calculated 0-0 ZPL is most red-shifted (Table 4.2)

ii) the dipole moment $|\Delta\mu| = \mu(S_1) - \mu(S_0)$ has the highest value, although lower than

| $Site$ | | $a-axis$ | $b-axis$ | $c-axis$ | $\|\mu\|$ |
|---|---|---|---|---|---|
| | $\mu(S_0 \rightarrow S_1)$ | 0.274 | −9.43 | −0.216 | 9.436 |
| **bbb** | $\mu(S_0)$ | −0.330 | −0.108 | −0.095 | 0.360 |
| $\lambda(0,0)$ = | $\mu(S_1)$ | −0.354 | −0.106 | −0.102 | 0.383 |
| 603.7 $nm$ | $\mu(S_1) - \mu(S_0)$ | −0.024 (−0.004) | 0.003 (−0.050) | −0.007 (0.001) | 0.023 (0.050) |
| | $\mu(S_0 \rightarrow S_1)$ | 0.384 | 8.020 | −4.649 | 9.278 |
| **bbc** | $\mu(S_0)$ | 0.456 | 0.013 | −1.756 | 1.815 |
| $\lambda(0,0)$ = | $\mu(S_1)$ | 0.429 | −0.062 | −1.648 | 1.704 |
| 607.1 $nm$ | $\mu(S_1) - \mu(S_0)$ | −0.027 (−0.064) | −0.074 (−0.102) | 0.108 (0.182) | 0.111 (0.218) |
| | $\mu(S_0 \rightarrow S_1)$ | −1.642 | 6.783 | 6.329 | 9.422 |
| **bcb'** | $\mu(S_0)$ | −0.478 | 0.303 | −0.414 | 0.701 |
| $\lambda(0,0)$ = | $\mu(S_1)$ | −0.530 | 0.301 | −0.437 | 0.750 |
| 604.1 $nm$ | $\mu(S_1) - \mu(S_0)$ | −0.052 (0.016) | −0.002 (0.001) | −0.023 (0.006) | 0.049 (0.016) |

Table 4.2.: Results of the ONIOM(B3LYP/6-31G(d,p):PM3) calculations for terrylene embedded in the considered cavities in the BTBT crystal. The quantity $\lambda(0,0)$ is the energy of the (0,0) transition with the zero-point energy correction (more details in table 3), $\mu(S_0 \rightarrow S_1)$, $\mu(S_0)$ and $\mu(S_1)$ are the dipole moments (in Debye) for the $S_0 \rightarrow S_1$ transition, and in the $S_0$ and $S_1$ states. Their components are presented along the crystal axes. For isolated terrylene $\lambda(0,0)$ = 604.3 nm and $\mu(S_0 \rightarrow S_1)$ = 9.443 D. In the rows for $\mu(S_1) - \mu(S_0)$ we show, between parentheses, the results of calculations with use of the simple but uniform B3LYP/3-21G method for the whole system (taken in the geometries optimized by ONIOM).



| | **isolated** | **bbb** | **bbc** | **bcb'** |
|---|---|---|---|---|
| *Transition energies from $S_0$ state ($nm$)* | | | | |
| $S_1$ | 554.7 | 554.8 | 561.7 | 558.1 |
| $T_1$ | 1221.8 | 1221.8 | 1259 | 1240.3 |
| $T_2$ | 549.6 | 549.7 | 552.5 | 551.9 |
| *SOC matrix elements ($cm^{-1}$) between $T_i$ and $S_k$* | | | | |
| $T_1/S_0$ | 0.0 | 0.16 (0.27) | 0.58 (0.19) | 0.12 (0.17) |
| $T_1/S_1$ | 0.0 | 0.00 | 0.00 | 0.02 (0.00) |
| $T_2/S_0$ | 0.0 | 0.16 (0.27) | 0.40 (0.34) | 0.33 (0.09) |
| $T_2/S_1$ | 0.0 | 0.04 (0.25) | 0.26 (0.24) | 0.07 (0.30) |

Table 4.3.: $H_{SO}$- Spin-orbit coupling matrix elements between the singlet and triplet states. In parenthesis we show the fraction of the z-component relative to the x and y components: $H_{SO,z}/H_{SO,xy}$.

the experimentally determined 0.28 ± 0.09 D (0.111 D obtained by the ONIOM method, and 0.218 D by using simple B3LYP/3-21G). In addition, the dipole vector has the highest value along the crystallographic axes b and c (Table 4.2), as suggested from the experiment. The calculated in-plane dipole vector orients about 30° with the c-axis, which indicates that the orientations found for the dipole vectors center around the crystallographic axes drawn in Figure 4.10c, with possibly four distributions resulting from the four possible, and spectroscopically

| *Site* | *Dipole Moment* | $\|\mu\|$ (*Debye*) | *X* | *Y* | *Z* |
|---|---|---|---|---|---|
| *Isolated* | $\mu(S_0 \rightarrow S_1)$ | 9.4430 | 0.0000 | 9.4430 | 0.0000 |
| *bbb* | $\mu(S_0 \rightarrow S_1)$ | 9.4346 | 0.0008 | −9.4346 | 0.0086 |
| | $\mu(S_0)$ | 0.0299 | −0.0016 | −0.0018 | −0.0298 |
| | $\mu(S_1)$ | 0.0401 | −0.0255 | 0.0025 | −0.0308 |
| *bbc* | $\mu(S_0 \rightarrow S_1)$ | 9.2768 | 0.0043 | 9.2768 | 0.0053 |
| | $\mu(S_0)$ | 0.3745 | −0.0060 | −0.0244 | 0.3736 |
| | $\mu(S_1)$ | 0.3275 | −0.0118 | −0.0145 | 0.3269 |
| *bcb′* | $\mu(S_0 \rightarrow S_1)$ | 9.4219 | 0.0023 | 9.4219 | 0.0279 |
| | $\mu(S_0)$ | 0.0428 | 0.0033 | 0.0418 | 0.0086 |
| | $\mu(S_1)$ | 0.0596 | 0.0216 | 0.0544 | 0.0046 |

Table 4.4.: Components of the dipole moments for terrylene taken from the sites and shown in the standard XYZ orientation (XY is the plane of Tr, Y is the direction of the long axis)

equivalent, in-plane orientations of the bbc site.

iii) Although the transition dipole moment vector is mostly aligned with the crystallographic b-axis, the bent structure of terrylene creates an angle of about 30° with this axis b. However, the only possible insertion that follows exactly the b-axis is site bbb, but the centrosymmetric arrangement of host molecules around terrylene in this site would lead to an effective zero dipole moment. The width of the distribution in Figure 4.11c does not exclude the possibility of a small angle of the transition moment with the b axis.

iv) The highest spin-orbit coupling was calculated for the site bbc.

## 4.4. CONCLUSION

Terrylene molecules embedded in a single crystal of BTBT possess favourable spectroscopic properties in terms of homogeneous linewidths and spectral stability. Furthermore, the studies we performed on the red-most spectroscopic site show that the host matrix induces a broken symmetry of the otherwise centrosymmetric terrylene, giving rise to a net in-plane dipole moment of $0.28 \pm 0.09$ Debye oriented in four in-plane directions. Although the induced net dipole moment could be classified as moderate, when for example compared to dibenzoterrylene (DBT) in 2,3-dibromonapthalene, the magnitude of the dipole vector is still remarkable and might point to a strong influence of the sulphur atoms on the charge distributions in the ground and excited state. For DBT in DBN it was found that mostly the side wings of DBT, which terrylene lacks, were responsible for the induced dipole through the host's bromine atoms.[4] In the case of the BTBT host, the effect of the sulphur atoms on the guest molecule could perhaps be strengthened by replacing terrylene with DBT.

Our reported method on the control of the electric fields' direction, applicable to any crystal, makes it possible to determine the dipole vector for each molecule individually,

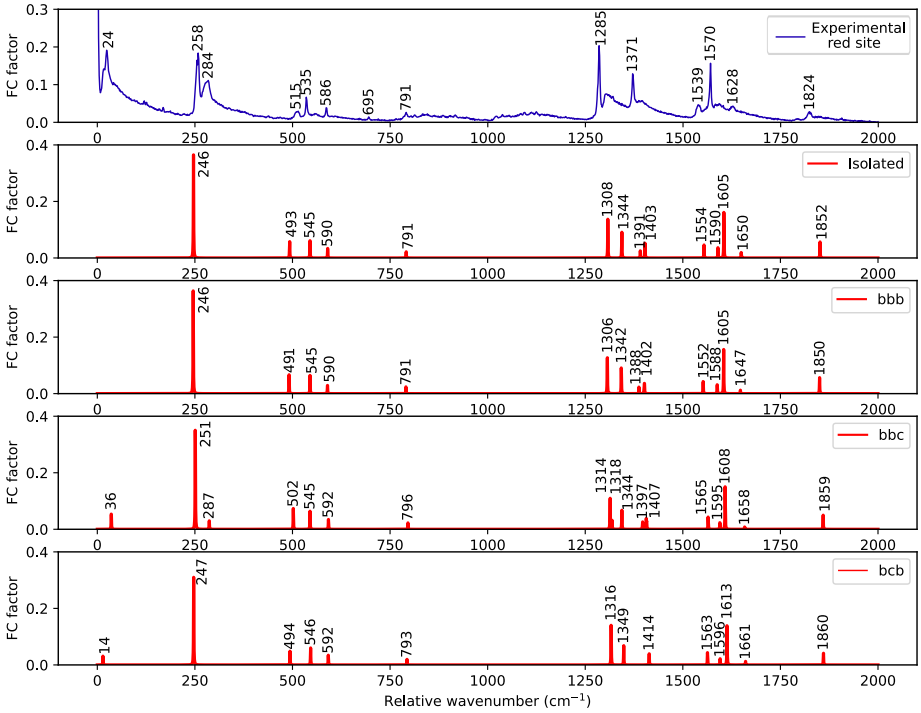


Figure 4.14.: Spectroscopic data for terrylene optimised in the BTBT crystal as a result of calculations by the ONIOM(B3LYP/6-31G(d,p):PM3) method (data in red). The calculations are compared to the experimental data of Figure 4.1 (data in blue)

which would make the use of these molecules for mapping electric fields, by direction and magnitude, or tracing charges, more reliable. In the future, the electric field control could be extended to three dimensions, by using the substrate's p-doped silicon layer as an additional electrode and an ITO cover glass as a top electrode for out-of-plane measurements of the dipole. Moreover, the good hole-conduction properties of BTBT and linear response of molecules to electric field, makes this an interesting system for the study of the injection of charges, for example by a field-effect transistor configuration.[35]

# REFERENCES


(1) Davila, H. V.; Salzberg, B. M.; Cohen, L. B.; Waggoner, A. S. *Nature New Biology* **1973**, *241*, 159–160.

(2) Marchetti, A. P.; Scozzafava, M.; Young, R.-H. *Chemical Physics Letters* **1977**, *51*, 3.

(3) Faez, S.; Verhart, N. R.; Markoulides, M.; Buda, F.; Gourdon, A.; Orrit, M. *Faraday Discussions* **2015**, *184*, 251–262.

(4) Moradi, A.; Ristanović, Z.; Orrit, M.; Deperasińska, I.; Kozankiewicz, B. *ChemPhysChem* **2019**, *20*, 55–61.

(5) Orrit, M.; Bernard, J.; Zumbusch, A. *Chemical Physics Letters* **1992**, *196*, 6.

(6) Fleury, L.; Zumbusch, A.; Orrit, M.; Brown, R.; Bernard, J. *Journal of Luminescence* **1993**, *56*, 15–28.

(7) Plakhotnik, T. *ChemPhysChem* **2006**, *7*, 1699–1704.

(8) Plakhotnik, T. *Journal of Luminescence* **2007**, *127*, 235–238.

(9) Faez, S.; van der Molen, S. J.; Orrit, M. *Physical Review B* **2014**, *90*, 205405.

(10) Rühl, M.; Lehmeyer, J.; Nagy, R.; Weisser, M.; Bockstedte, M.; Krieger, M.; Weber, H. B. *New Journal of Physics* **2021**, *23*, 073002.

(11) Bassett, L. C.; Heremans, F. J.; Yale, C. G.; Buckley, B. B.; Awschalom, D. D. *Physical Review Letters* **2011**, *107*, 266403.

(12) Deperasińska, I.; Banasiewicz, M.; Gawryś, P.; Morawski, O.; Olas, J.; Kozankiewicz, B. *The Journal of Chemical Physics* **2021**, *155*, 034504.

(13) Nicolet, A.; Kol'chenko, M. A.; Kozankiewicz, B.; Orrit, M. *The Journal of Chemical Physics* **2006**, *124*, 164711.

(14) Navarro, P.; Tian, Y.; van Stee, M.; Orrit, M. *ChemPhysChem* **2014**, *15*, 3032–3039.

(15) Kummer, S.; Basché, T.; Bräuchle, C. *Chemical Physics Letters* **1994**, *229*, 309–316.

(16) Deperasińska, I.; Kozankiewicz, B. *Chemical Physics Letters* **2017**, *684*, 208–211.

(17) Gorshelev, A. A.; Naumov, A. V.; Eremchev, I. Y.; Vainer, Y. G.; Kador, L.; Köhler, J. *ChemPhysChem* **2010**, *11*, 182–187.

(18) Colautti, M.; Piccioli, F. S.; Ristanović, Z.; Lombardi, P.; Moradi, A.; Adhikari, S.; Deperasinska, I.; Kozankiewicz, B.; Orrit, M.; Toninelli, C. *ACS Nano* **2020**, *14*, 13584–13592.

(19) Kummer, S.; Basche, T. *The Journal of Physical Chemistry* **1995**, *99*, 17078–17081.

(20) Plakhotnik, T.; Moerner, W. E.; Palm, V.; Wild, U. P. *Optics Communications* **1995**, *114*, 83–88.

(21) Verberk, R.; Orrit, M. *The Journal of Chemical Physics* **2003**, *119*, 2214–2222.

(22) Basché, T.; Moerner, W. E. *Nature* **1992**, *355*, 335–337.

(23) Kol'chenko, M. A. *Optics and Spectroscopy* **2005**, *98*, 681.

(24) Keum, C.-M.; Liu, S.; Al-Shadeedi, A.; Kaphle, V.; Callens, M. K.; Han, L.; Neyts, K.; Zhao, H.; Gather, M. C.; Bunge, S. D.; Twieg, R. J.; Jakli, A.; Lüssem, B. *Scientific Reports* **2018**, *8*, 699.

(25) Wolf, H. C. *Zeitschrift für Naturforschung A* **1958**, *13*, 414–419.

(26) Nakada, I. *Journal of the Physical Society of Japan* **1962**, *17*, 113–118.

(27) Lawetz, V.; Orlandi, G.; Siebrand, W. *The Journal of Chemical Physics* **1972**, *56*, 4058–4072.

(28) Patterson, F. G.; Lee, H. W. H.; Wilson, W. L.; Fayer, M. D. *Chemical Physics* **1984**, *84*, 51–60.

(29) Brouwer, A. C. J.; Groenen, E. J. J.; Schmidt, J. *Physical Review Letters* **1998**, *80*, 3944–3947.

(30) Liu, X.; Su, X.; Livache, C.; Chamoreau, L.-M.; Sanaur, S.; Sosa-Vargas, L.; Ribierre, J.-C.; Kreher, D.; Lhuillier, E.; Lacaze, E.; Mathevet, F. *Organic Electronics* **2020**, *78*, 105605.

(31) Aubret, A.; Orrit, M.; Kulzer, F. *ChemPhysChem* **2019**, *20*, 345–355.

(32) Nicolet, A. A. L.; Hofmann, C.; Kol'chenko, M. A.; Kozankiewicz, B.; Orrit, M. *ChemPhysChem* **2007**, *8*, 1215–1220.

(33) Frisch, M. J.; Trucks, G. W.; Schlegel, H. B.; Scuseria, G. E.; Robb, M. A.; Cheeseman, J. R.; Scalmani, G.; Barone, V.; Petersson, G. A.; Nakatsuji, H.; Li, X.; Caricato, M.; Marenich, A. V.; Bloino, J.; Janesko, B. G.; Gomperts, R.; Mennucci, B.; Hratchian, H. P.; Ortiz, J. V.; Izmaylov, A. F.; Sonnenberg, J. L.; Williams; Ding, F.; Lipparini, F.; Egidi, F.; Goings, J.; Peng, B.; Petrone, A.; Henderson, T.; Ranasinghe, D.; Zakrzewski, V. G.; Gao, J.; Rega, N.; Zheng, G.; Liang, W.; Hada, M.; Ehara, M.; Toyota, K.; Fukuda, R.; Hasegawa, J.; Ishida, M.; Nakajima, T.; Honda, Y.; Kitao, O.; Nakai, H.; Vreven, T.; Throssell, K.; Montgomery Jr., J. A.; Peralta, J. E.; Ogliaro, F.; Bearpark, M. J.; Heyd, J. J.; Brothers, E. N.; Kudin, K. N.; Staroverov, V. N.; Keith, T. A.; Kobayashi, R.; Normand, J.; Raghavachari, K.; Rendell, A. P.; Burant, J. C.; Iyengar, S. S.; Tomasi, J.; Cossi, M.; Millam, J. M.; Klene, M.; Adamo, C.; Cammi, R.; Ochterski, J. W.; Martin, R. L.; Morokuma, K.; Farkas, O.; Foresman, J. B.; Fox, D. J. Gaussian 16 Rev. C.01, Wallingford, CT, 2016.

(34) Neese, F. *WIREs Computational Molecular Science* **2018**, *8*, e1327.

(35) Nicolet, A. A. L.; Kol'chenko, M. A.; Hofmann, C.; Kozankiewicz, B.; Orrit, M. *Physical Chemistry Chemical Physics* **2013**, *15*, 4415–4421.